Proceedings, 5th AOSFST, Newcastle, Australia, 2001
Editors: M.A. Delichatsios, B.Z. Dlugogorski and E.M. Kennedy

ALIGNMENT EFFECT ON THE STRUCTURE OF METHANE – AIR COUNTERFLOW DIFFUSION FLAMES

C. Luo, B. Z. Dlugogorski, E. M. Kennedy, and B. Moghtaderi

Department of Chemical Engineering, The University of Newcastle

AUSTRALIA

ABSTRACT

A three dimensional model was developed to describe the scalar structure which exists in a countercurrent turbulent diffusion flame. The model was solved numerically by combining CHEMKIN thermochemical and transport databases within the CFX4.3 software. The distance between the axis of the upper oxidiser duct and the lower fuel duct, termed eccentricity, was used to describe the severity of the torch misalignment. Due to the misalignment, the original horizontal flat flame becomes inclined and distorted. The flame structure along the centre line of the torch is not sensitive to eccentricity. However, the cross sectional contours of velocity, density and species mass fractions illustrate significant effect on eccentricity. Finally, the paper makes suggestions for experimental verification of the alignment of the counterflow burner in experiments and examines the validity of constant $1/r(\partial p/\partial r)$ assumption in a misaligned burner.

Keywords: Turbulent diffusion flame, counterflow burner, methane-air combustion, opposed flow flames.

INTRODUCTION

Counterflow burners provide standard geometry for studying combustion and extinction processes in diffusion and premixed flames. Over the last four decades, counterflow burners have been applied to investigate both laminar and turbulent flames[7,9,10]. Opposed flow burners display superior flame stability and minimise the effect of solid surfaces on a flame structure, allowing a researcher to focus on flame properties. Usually, one studies only the flame behaviour along the torch centre line[8,14].

Parameters which govern the behaviour of countercurrent flames include burner geometry (e.g. nozzle diameters, gap between the nozzles), species composition, flow rate of fuel, oxidant and shroud gas, as

well as turbulent intensities of incoming gases. This paper concentrates on the effect of misalignment of the upper and lower ducts on properties of countercurrent turbulent diffusion flames.

Since Potter and Butler introduced the opposed-jet setup in 1958, numerical studies aiming at revealing the flame structure have focused on a one-dimensional model. Dixon-Lewis et al.[4] adopted the boundary-layer equations for describing the variation of density, velocity, pressure, energy and species mass fractions, with the entire flow field being defined by one global parameter, the potential-flow velocity gradient. The disadvantage of this approach is that it assumes that the two point sources for the oxidiser and fuel streams, respectively, are positioned far from the stagnant mid-plane necessitating non-zero radial velocities at the exits from the upper and lower ducts. Later, Kee et al.[7] and Dixon-Lewis[4] removed this drawback by introducing a stream function $\psi(r, x) = r^2 V_x(x)$ and assuming that all scalar properties depend only on the axial position. Based on these assumptions, the well-known and still popular OPPDIF program was developed.

With respect to two dimensional numerical studies, Takagi et al.[15] discretised the governing equations using upwind difference scheme for convective terms and central difference scheme for diffusion terms to investigate strained non-premixed flames affected by flame curvature and preferential diffusion. In 1998, Frouzakis et al.[6] carried out two-dimensional simulations of a hydrogen-air laminar opposed-jet diffusion flame, and compared their results with those of 1D axisymmetric model. However, Takagi et al. and Frouzakis et al. did not provide quantitative comparison with experimental data, and did not carry out a systematic investigation of the counterflow diffusion flame structure. The open literature appears to contains no model of 3D countercurrent flame structure, necessary to study misalignment of the burner's ducts.

The alignment of the burner's ducts has been considered as one of the most important sources of inaccuracies in experimental results. Experimentalists often question themselves about the types of errors caused by misalignment and about a simple procedure to align the torch well. To address these issues, a 3D mathematical description of counterflow burner capable of modelling the misalignment effects has been developed. The model has been verified against available experimental data[14].

The current paper presents axial and radial profiles as well as contours of temperature, velocity and species molar fractions for various misalignment cases of methane-air counterflow diffusion flames. The results demonstrate a comprehensive aerothermochemical flame structure as a consequence of misalignment. Based on the modelling results, the paper makes suggestions for ways to verify the burner alignment in experiments.

Mathematical description

In this section, a brief review is given of the mathematical formulation of the model in cylindrical coordinates. The model uses three-dimensional Favré-averaged equations of conservation of mass, momentum (Navier-Stokes), gas species and enthalpy. Turbulence and combustion are modelled via the k-ε closure and one step global reaction kinetics. The conservation equations for the three velocity components (V_x, V_r and V_θ), turbulence kinetic energy (k), turbulence energy dissipation (ε), enthalpy (h) and species concentrations are cast into the following form:

$$\frac{\partial}{\partial t}(\rho\phi)+\frac{1}{r}\frac{\partial(r\rho V_r\phi)}{\partial r}+\frac{\partial(\rho V_x\phi)}{\partial x}+\frac{1}{r}\frac{\partial(\rho V_\theta\phi)}{\partial\theta}$$
$$=\frac{1}{r}\frac{\partial}{\partial r}\left(\Gamma_\phi\frac{r\partial\phi}{\partial r}\right)+\frac{1}{r}\frac{\partial}{\partial\theta}\left(\Gamma_\phi\frac{1}{r}\frac{\partial\phi}{\partial\theta}\right)+\frac{\partial}{\partial x}\left(\Gamma_\phi\frac{\partial\phi}{\partial x}\right)+S_\phi \quad (1)$$

where ϕ denotes the conserved variable, ρ stands for density, Γ_ϕ is the diffusion coefficient for ϕ and S_ϕ signifies the source term; ϕ = 1 gives the continuity equation. The governing equations are discretised on a grid using the finite volume approach and the resulting equations are solved by SIMPLEC method. Buoyancy terms were not included in the governing equations; this simplification does not affect the scalar structure along the centre line.

The diffusion coefficients and source terms are as follows:

For V_x-equation:

$$\Gamma_\phi=\mu,\ S_\phi=\frac{\partial}{\partial x}\left(\mu\frac{\partial V_x}{\partial x}\right)+\frac{1}{r}\frac{\partial}{\partial r}\left(r\mu\frac{\partial V_r}{\partial x}\right)+\frac{1}{r}\frac{\partial}{\partial\theta}\left(\mu\frac{\partial V_\theta}{\partial x}\right)-\frac{\partial p}{\partial x};$$

For V_r-equation:

$$\Gamma_\phi=\mu,\ S_\phi=\frac{\partial}{\partial x}\left(\mu\frac{\partial V_x}{\partial r}\right)+\frac{1}{r}\frac{\partial}{\partial r}\left(r\mu\frac{\partial V_r}{\partial r}\right)+\frac{1}{r}\frac{\partial}{\partial\theta}\left(r\mu\frac{\partial}{\partial x}\left(\frac{V_\theta}{r}\right)\right)-\frac{2\mu}{r^2}\frac{\partial V_\theta}{\partial\theta}-$$
$$\frac{2\mu V_r}{r^2}+\frac{\rho V_\theta{}^2}{r}-\frac{\partial p}{\partial r};$$

For V_θ-equation:

$$\Gamma_\phi=\mu,\ S_\phi=\frac{\partial}{\partial x}\left(\frac{\mu}{r}\frac{\partial V_x}{\partial\theta}\right)+\frac{1}{r}\frac{\partial}{\partial r}\left(r\mu\left(\frac{1}{r}\frac{\partial V_r}{\partial\theta}-\frac{V_\theta}{r}\right)\right)-\rho\frac{V_\theta V_r}{r}+$$
$$\frac{1}{r}\frac{\partial}{\partial\theta}\left(\frac{\mu}{r}\left(\frac{\partial V_\theta}{\partial\theta}+2V_r\right)\right)+\frac{\mu}{r}\left(\frac{\partial V_\theta}{\partial r}+\frac{\partial V_r}{r\partial\theta}-\frac{V_\theta}{r}\right)-\frac{\partial p}{\partial r}\ .$$

For species mass fraction, $\Gamma_\Phi=\Gamma_i+\frac{\mu}{\sigma_i}$, where σ_i is the corresponding species turbulent Prandtl number and Γ_i denotes the species diffusivity, $S_\phi=W_i n_i R$, in which W_i is the molecular weight of species i, n_i is the overall stoichiometric coefficient of species i and R is the reaction rate.

The following set of equations are used for the effective viscosity:

$$\mu=\mu_m+\mu_t\ ,$$

$$\mu_t = C_\mu \rho \frac{k^2}{\varepsilon} \tag{2}$$

$$\frac{\partial(\rho k)}{\partial t} + \frac{\partial}{\partial x}\left(\rho k V_x - (\mu_m + \frac{\mu_t}{\sigma_k})\frac{\partial k}{\partial x}\right) + \frac{1}{r}\frac{\partial}{\partial r}\left[r\left(\rho k V_r - (\mu_m + \frac{\mu_t}{\sigma_k})\frac{\partial k}{\partial r}\right)\right] + \frac{1}{r}\frac{\partial}{\partial \theta}\left[\left(\rho k V_\theta - (\mu_m + \frac{\mu_t}{\sigma_k})\frac{1}{r}\frac{\partial k}{\partial \theta}\right)\right] = P + G - \rho\varepsilon \tag{3}$$

$$\frac{\partial(\rho \varepsilon)}{\partial t} + \frac{\partial}{\partial x}\left(\rho \varepsilon V_x - (\mu_m + \frac{\mu_t}{\sigma_\varepsilon})\frac{\partial \varepsilon}{\partial x}\right) + \frac{1}{r}\frac{\partial}{\partial r}\left[r\left(\rho k V_r - (\mu_m + \frac{\mu_t}{\sigma_\varepsilon})\frac{\partial \varepsilon}{\partial r}\right)\right] + \frac{1}{r}\frac{\partial}{\partial \theta}\left[\left(\rho k V_\theta - (\mu_m + \frac{\mu_t}{\sigma_\varepsilon})\frac{\partial \varepsilon}{\partial \theta}\right)\right] = C_1 \frac{\varepsilon}{k}\left(P + C_3 \max(G,0)\right) - C_2 \rho \frac{\varepsilon^2}{k} \tag{4}$$

where P is the shear production and G denotes production of the turbulent kinetic energy (k) and turbulent dissipation rate (ε) due to body force with C_1 = 1.44, C_2 = 1.92, C_3 = 0.0, σ_k = 1.0, $\sigma_\varepsilon = \frac{\kappa^2}{(C_2 - C_1)\sqrt{C_\mu}}$ in which von Kármán constant κ = 0.4187 and C_μ = 0.09.

Computational details

Figure 1(a) illustrates the computational domain considered in this study. Constant atmospheric pressure is imposed at the boundary planes Xf1 and Xf2 (Figure 1(b), away from the jet exits) and other scalars are set to fixed values at these boundaries. The Xf1 and Xf2 planes constitute far-field boundaries, so that the constant pressure assumption is a reasonable imposed condition. Following some experimental studies which employed a container filled with an inert gas to enclose the counterflow burner, the concentration of the inert gas (nitrogen) was set at 100% at far field (Xf1 and Xf2 planes). For a counterflow burner open to ambient, the air composition was specified at Xf1 and Xf2.

Specified velocity, temperature and species mass fractions are imposed at the fuel and oxidiser exits (boundary planes B1 and B2 in Figure 1(b)). The plug velocity distribution is set for B1 and B2, that is $u = V_0$ for r <7 mm for the lower (fuel) exit and $u = -V_0$ for $|r-e|$ <7 mm for the upper (oxidiser) exit. Here e stands for the eccentricity between the upper and lower burner duct exits. For the radial far-field boundary, the Neumann condition is imposed on velocity components, pressure, and species mass fractions.

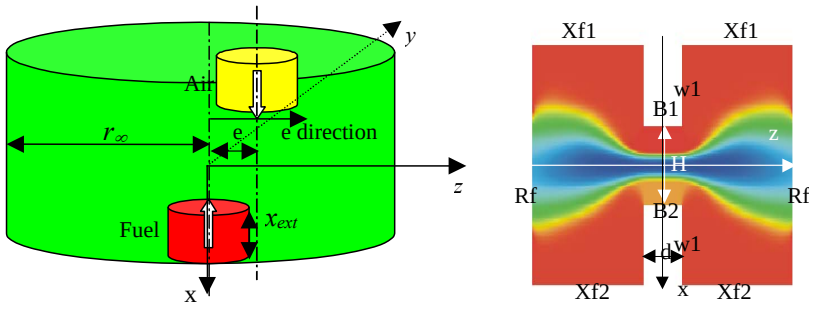

(a) (b)

Figure 1: (a) Configuration of the counterflow burner considered in this study and (b) *x-z* cross section of the computational domain.

Finer mesh is used within the jet region ($r < a$ and $-H/2 < x < H/2$) than elsewhere in the simulation domain. The initial condition for the velocity field involves stationary nitrogen gas for the enclosed burner and air for the open burner, across the entire computational domain. Both nitrogen and the air have an initial temperature of 300 K. The results reported here were obtained with 90 × 80 × 50 (axial × radial × azimuthal) grids, where axial distances Δx = 1 mm for grids 1 - 10 and 81 - 90, Δx = 0.3 - 0.9 and 0.9 - 0.3 mm for grids 11 - 15 and 76 - 80 respectively, Δx = 0.21667 mm for $-H/2<x<H/2$ (16 - 75), radial distances Δr = 0.175 mm for $r<a$ (1 - 40), Δr = 0.2 - 1.0 mm for grids 41 - 57, Δr = 1 mm for grids 58 - 80 and azimuthal distances $\Delta\theta$ = 0.12566 for K = 1, 50. Because the flame is thin along the axial direction, axial gradients near the flame are very large, suggesting that the finer axial grids are desired for improved accuracy. For examining the grid sensitivity, two cases were investigated with all computational parameters identical except for size of the axial cells $\Delta x_1 = 0.21667$ mm and $\Delta x_2 = 0.10$ mm. These computations led to almost identical axial and radial profiles of the studied variables. Consequently, in further calculations, an axial cell size of 0.21667 mm within the jet region ($-H/2<x<H/2$) was adopted.

The CFX software is installed on Sun SPARCstations at The University of Newcastle. On average, 3D computational case with 80 × 80 × 50 grids requires 3 to 4 days of CPU time. A converged solution is accepted once the global error in mass balance decreases to below 10^{-8}. This usually occurs after 800 iterations.

To investigate the effect of eccentricity on the flame structure, in the current paper presents three computational cases with eccentricity of 0, 1 and 2 mm. Following Sung et al.[14], the jets' exit diameters are set to 14 mm and the separation distance between the nozzles is taken as 13 mm, with the mid-plane located at x = 0 mm; that is, the fuel exit is 6.5 mm below and oxidiser exit 6.5 mm above with respect to the mid-plane. Note that, the x-axis points downward. The fuel and oxidiser streams respectively comprise 23% (volume) methane in nitrogen and 23% (volume) oxygen in nitrogen. Bedat et al.'s[2] one step global kinetic parameters for reaction $CH_4 + 2O_2 = 2H_2O + CO_2$ are adopted: $A = 4.4 \times 10^{17}$ (kmol/m^3)$^{-2}$ and $E_a = 2.1 \times 10^8$ J/kmol.

RESULTS AND DISCUSSION

Figures 2(a) and 2(b) present the axial velocity contours at *x*-*z* and *x*-*y* planes for e = 2 mm. It can be seen that the eccentricity leads to non-symmetrical axial velocity distribution only along the eccentricity direction (here the *z*-axis). Though, the velocity distribution remains symmetrical along the *y*-axis perpendicular to the direction of eccentricity. The axial velocity distributions at the mid-plane and at the oxidiser exit are shown in Figures 2(c) and 2(d), respectively. Note that the velocity scale is different for Figures 2(c) and 2(d), with the maximum speeds occurring at the *y*-*z* mid-plane. Certainly, this is not always the case. Sometimes, the maximum velocity is located at the upper and lower nozzle exits for flow rates smaller than those used to obtain results shown in Figure 2.

Figures 3 shows the speed contours for y = 0 (*x*-*z* plane) and z = 0 (*x*-*y* plane), clearly indicating that the inclination of the flame sheet increases with the eccentricity e. In the *x*-*y* cross section, the speed contours are symmetrical, although the upper jet diameter (corresponding to the cord of the inner circle along the *y* axis in Figure 2(d)) appears slightly smaller than that of the lower jet. It can also be seen that the maximum speed decreases slightly from 0.95 m/s for e = 1 mm to 0.83 m/s for e = 2 mm. To examine the radial velocity variations with eccentricity, Figure 4 compares v_z velocity contours for e = 2 mm with those for e = 1 mm.

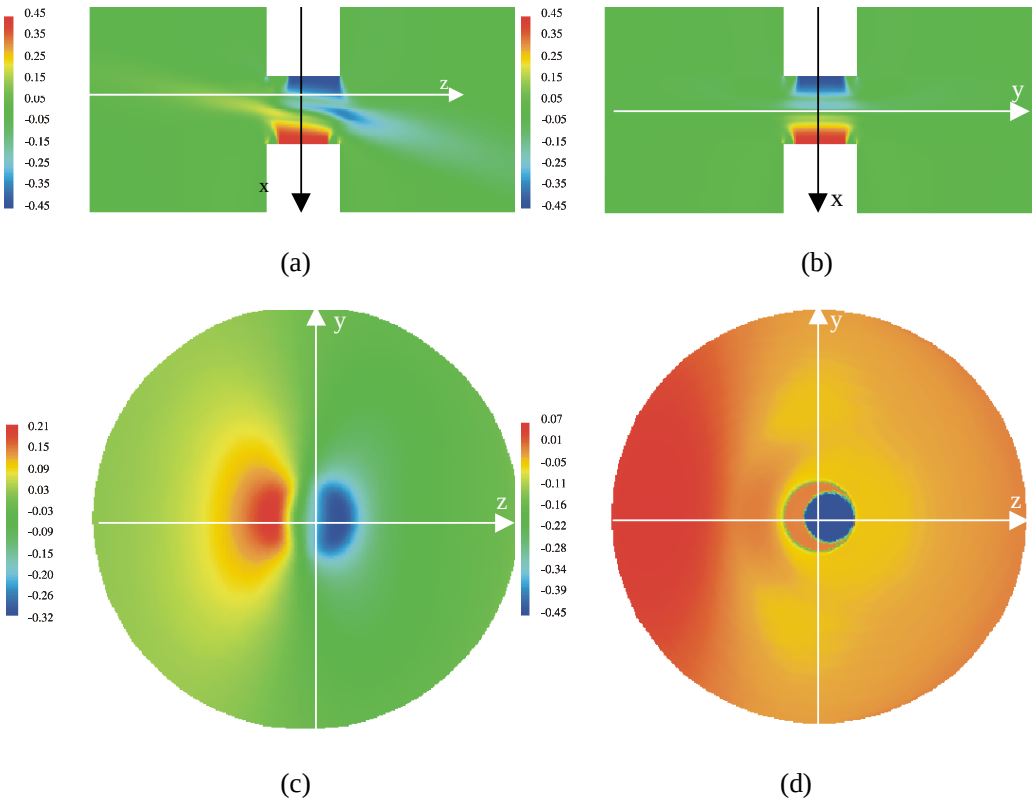

Figure 2: Axial velocity contours (in m/s) at: (a) *x*-*z* plane; (b) *x*-*y* plane; (c) *y*-*z* mid-plane; (d) cross section at the height of oxidiser exit for eccentricity e = 2 mm (V_0 = 0.45 m/s, H = 13 mm, d = 14 mm and 80 × 80 × 50 grids).

The fuel mass fraction contours for different cross sections are illustrated in Figure 5. The *x-z* cross-section contour demonstrates the lack of symmetry as a consequence of the ducts' misalignment. This is further corroborated in Figure 5(c), which illustrates a high CH_4 concentration along the negative *z*-axis, as the eccentricity increases. On the other hand, symmetry is preserved in the direction perpendicular to the direction of eccentricity as illustrated in Figure 5(b), as was also the case for the velocity contours.

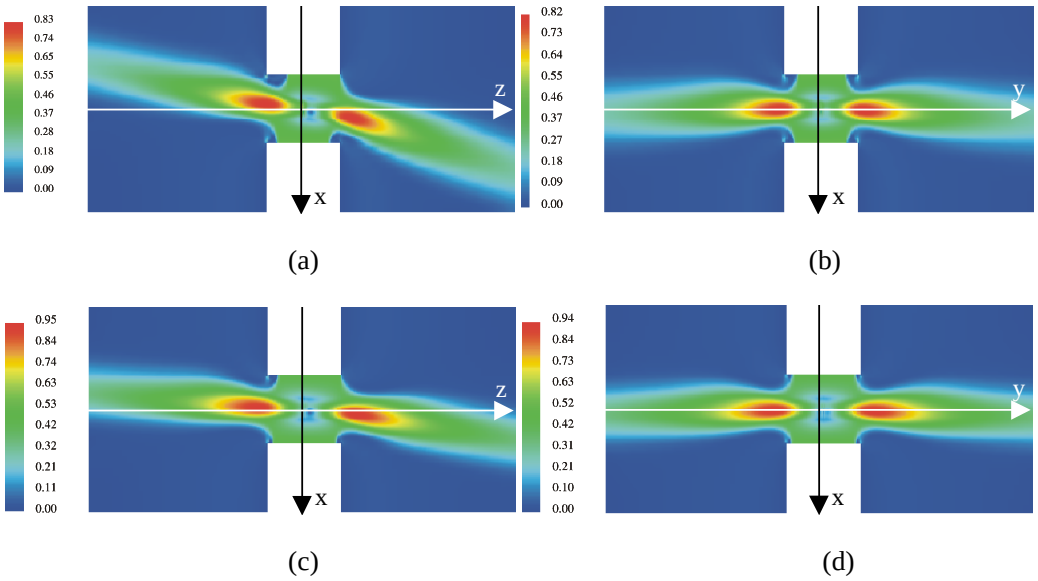

Figure 3: Speed contours (in m/s) on (a) *x-z* plane for e = 2 mm; (b) *x-y* plane for e = 2 mm; (c) *x-z* plane for e = 1 mm; (d) *x-y* plane for e = 1 mm (V_0 = 0.45 m/s, H = 13 mm, d = 14 mm and 80 × 80 × 50 grids).

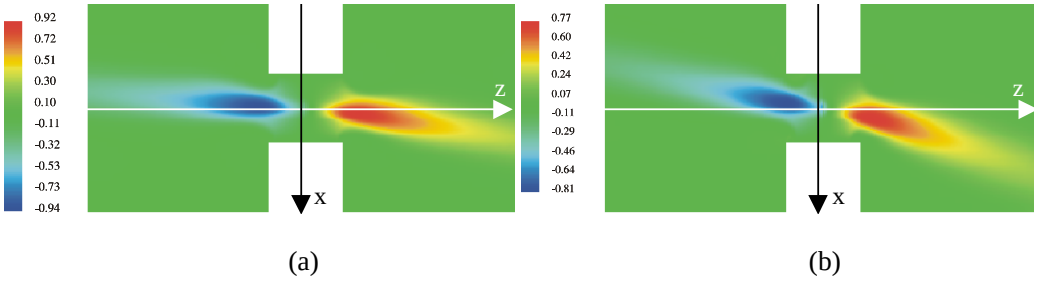

Figure 4: V_z velocity contours (in m/s) for (a) e = 1 and (b) e = 2 mm with V_0 = 0.45 m/s, H = 13 mm, d = 14 mm and 80 × 80 × 50 grids.

Figure 6 shows the mass fraction contours of one of the product gases, H_2O, for flames with and without eccentricity. By comparing Figures 6(c) with 6(d), it can be seen that, eccentricity reduces the width of the H_2O mass fraction contour in the z direction, though the extension of the contour in y direction is not affected. Since temperature, enthalpy, CO_2, turbulent intensity and turbulent dissipation rate are described by conservation equations that are similar in form to each other, the contours of these quantities are also similar. For this reason, Figure 7 only compares the density and enthalpy contours for eccentricity of 1 mm with those of eccentricity of 2 mm, in each case indicating steep inclination at higher eccentricity.

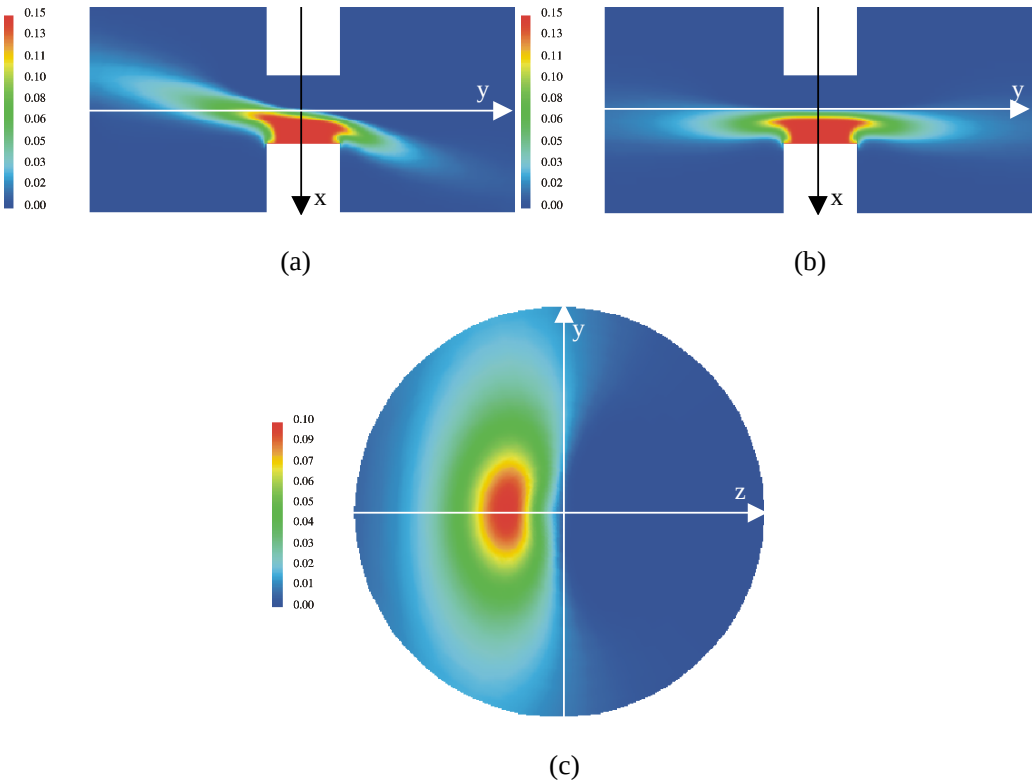

Figure 5: CH_4 mass fraction contours viewed from (a) x-z plane, (b) x-y plane and (c) y-z mid-plane for e = 2 with V_0 = 0.45 m/s, H = 13 mm, d = 14 mm and 80 × 80 × 50 grids.

To examine the response of the flame structure along the centre line to the eccentricity, Figure 8 presents axial profiles of the axial velocity component, H_2O mass fraction, temperature and reactant mass fraction for eccentricity of 0, 1 and 2 mm. It can be seen that the difference between e = 0 and e = 1 is very small, with the velocity peak moving closer toward the mid-plane as eccentricity increases. Also, all profiles including the one obtained from the one dimensional model (OPPDIF) are in reasonable agreement with each other. Figure 8(b) shows a similar comparison of the

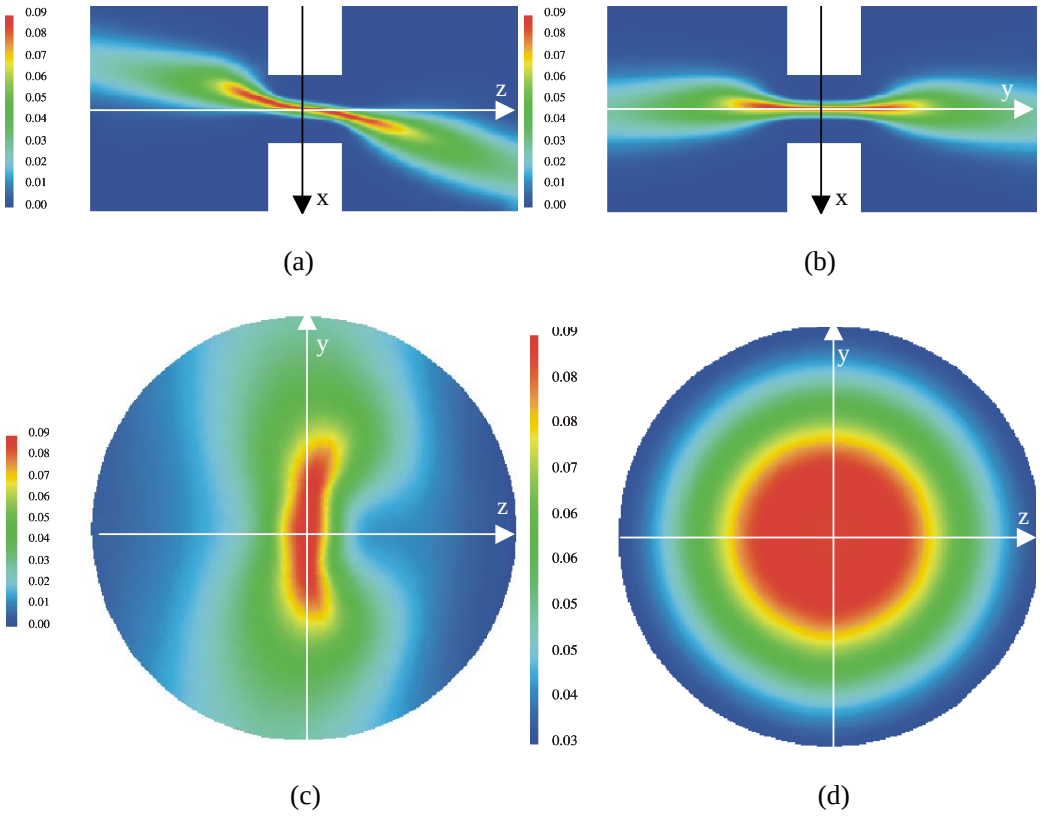

Figure 6: H_2O mass fraction contours on (a) *x*-*z* plane; (b) *x*-*y* plane; (c) *y*-*z* mid-plane for $e = 2$; (d) *y*-*z* mid-plane for symmetry case or $e = 0$ ($V_0 = 0.45$ m/s, $H = 13$ mm, $d = 14$ mm with $80 \times 80 \times 50$ grids).

H_2O mass fraction profiles along the centre axis, indicating good accord among the curves with the exception of the peak value at the mid-plane. Figure 9(c) presents a comparison of the axial temperature profiles for $e = 0$, 1, 2 with the spontaneous Raman scattering data of Sung et al.[14] again, showing the peak temperature difference of less than 100 K. The reactant mass fraction axial profiles are illustrated in Figure 8(d), demonstrating only minor differences. Therefore, it can be concluded that the scalar structure along the flame centre axis is not sensitive to eccentricity. However, this is not the case for the radial profiles, as illustrated in Figure 9.

Figure 9 presents profiles of the radial temperature, H_2O mass fraction and pressure for flames with and without eccentricity. Figure 9(a) demonstrates the symmetrical temperature profiles along the *y* direction for $e = 1$ mm and lack of symmetry along the *z*-axis; that is, along the axis of eccentricity. It can also be noticed that the flat portion of the temperature profiles along the *y* direction is narrower for $e = 1$ mm in comparison with the case of no eccentricity. Similar remarks can be drawn for the H_2O mass fraction profiles in the radial direction shown in Figure 9(b).

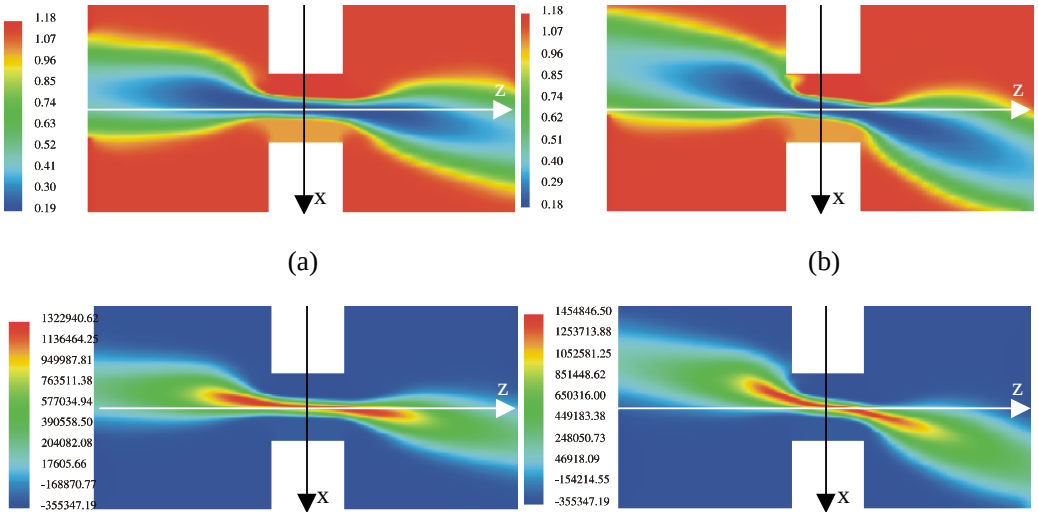

Figure 7: *X-z* contours of (a) density (in kg/m^3) for e = 1 mm; (b) density for e = 2 mm; (c) enthalpy (unit: J) for e = 1 mm; (d) enthalpy for e = 2 mm (V_0 = 0.45 m/s, H = 13 mm, d = 14 mm with 80 × 80 × 50 grids).

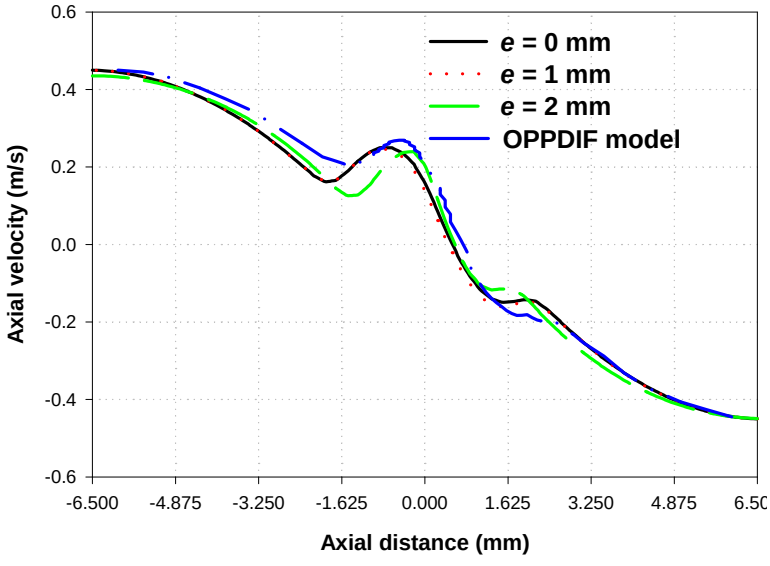

(a)

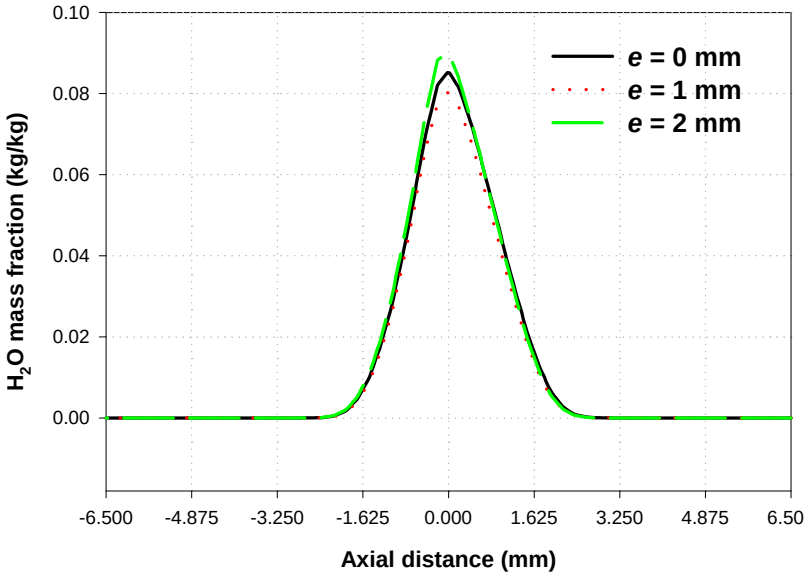
0.10
0.08
0.06
0.04
0.02
0.00
H2O mass fraction (kg/kg)
e = 0 mm
e = 1 mm
e = 2 mm
-6.500
-4.875
-3.250
-1.625
0.000
1.625
3.250
4.875
6.50
Axial distance (mm)

(b)

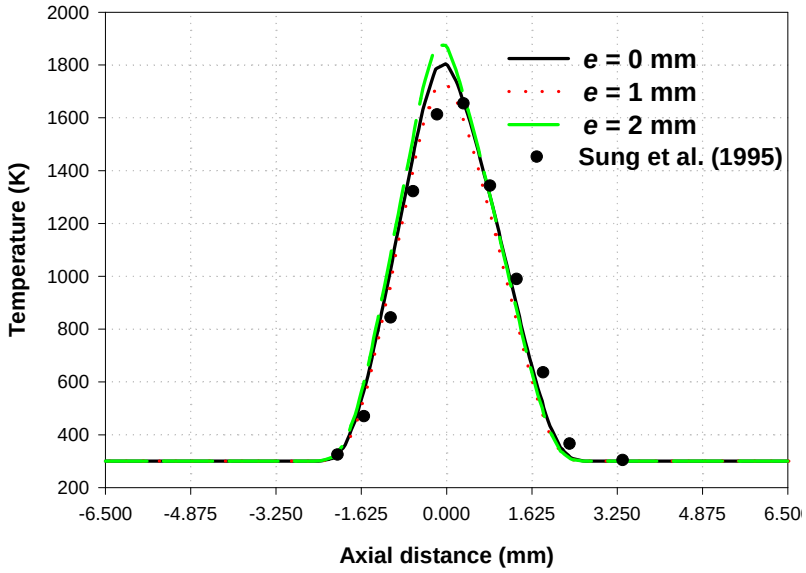
2000
1800
1600
1400
1200
1000
800
600
400
200
Temperature (K)
e = 0 mm
e = 1 mm
e = 2 mm
Sung et al. (1995)
-6.500
-4.875
-3.250
-1.625
0.000
1.625
3.250
4.875
6.50
Axial distance (mm)

(c)

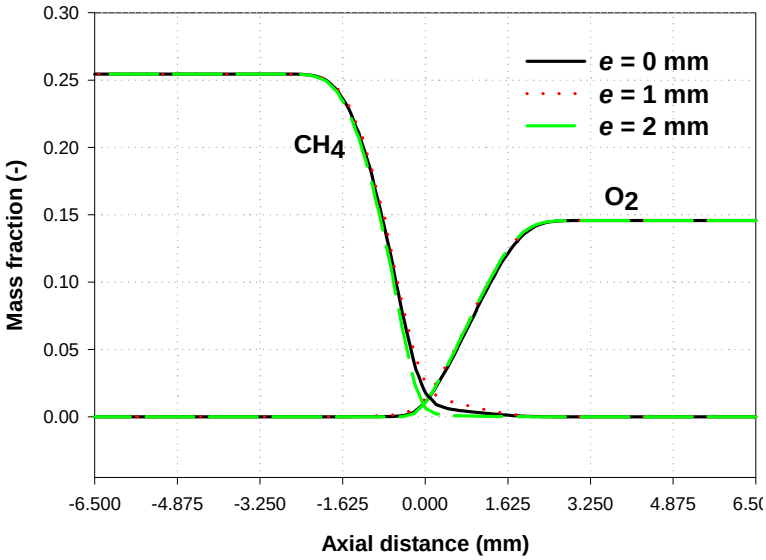

(d)

Figure 8: Axial profiles of (a) velocity, (b) H_2O mass fraction, (c) temperature and (d) reactant mass fraction along the central symmetry axis with variations of deviation e for V_0 = 0.45 m/s, H = 13 mm, d = 14 mm and 80 × 80 × 50 grids.

Figure 10 presents the radial profiles of relative pressure, defined as the difference between the absolute and atmosphere pressure, fitted with a quadratic polynomial. In this figure, the dot symbols represent the calculated values for e = 0 and 1 mm respectively. It can be seen that $1/r(\partial p/\partial r)$ is -6.6×10^8 Pa/m^2 for e = 0 and $-1/r(0.0041+0.0056r) \times10^{11}$ Pa/m^2 for e = 1 mm, demonstrating that the assumption of constant $1/r(\partial p/\partial r)$ adopted in the OPPDIF code does not hold for misaligned counterflow flames.

From the proceeding analyses of aligned and misaligned flames, it is clear that an aligned burner produces symmetrical flames but only along the centre axis. An experimentalist may use this characteristic to estimate the degree of torch misalignment. Alternatively, one can measure temperature or concentration profiles. Radial symmetry of the measured profiles implies good alignment.

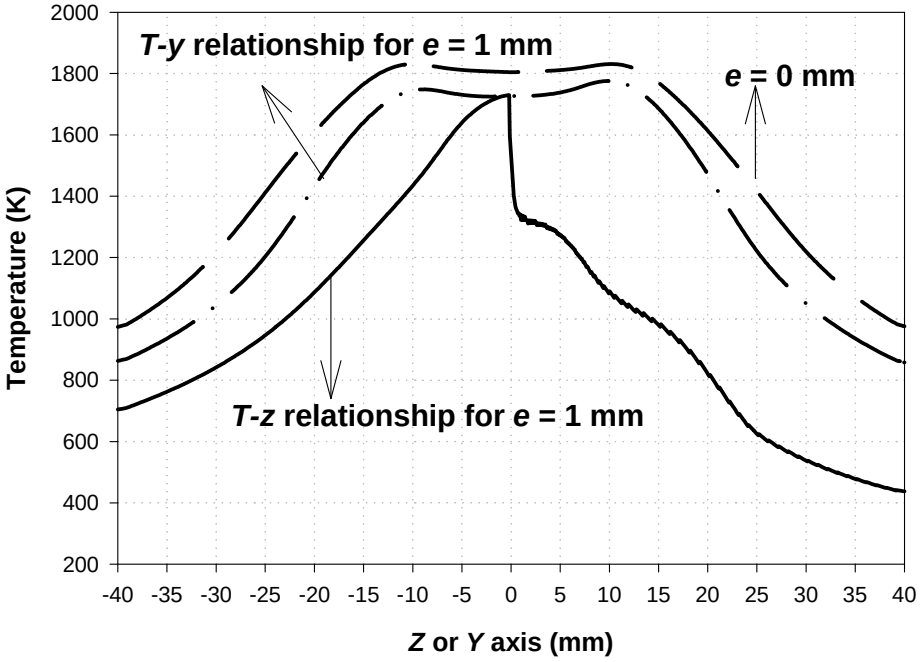

(a)

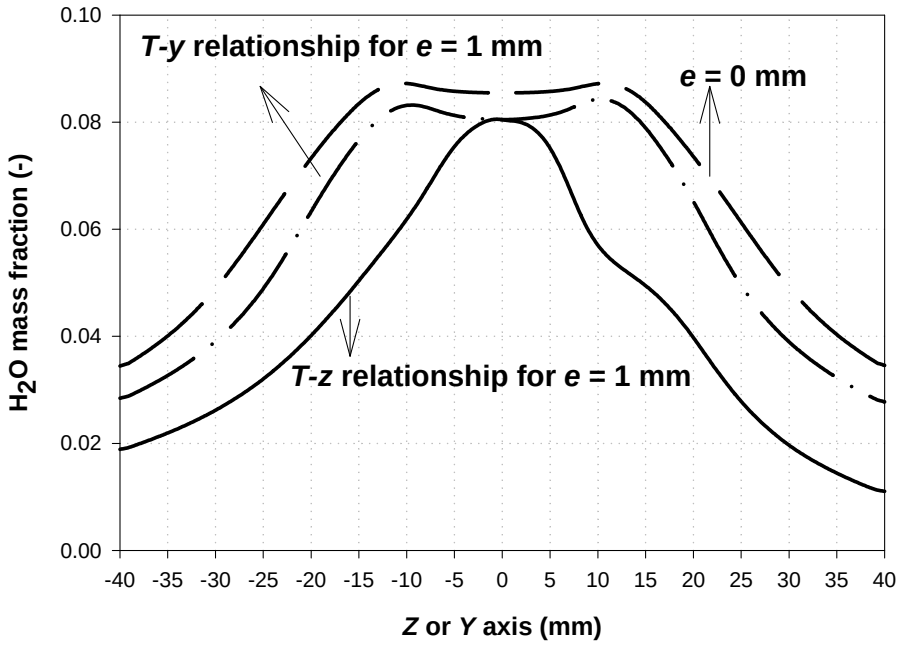

(b)

Figure 9: Profiles of (a) temperature (b) H_2O mass fraction along y and z directions at mid-plane between the upper and lower jet exits for V_0 = 0.45 m/s, H = 13 mm, d = 14 mm, e = 1 mm with 80 × 80 × 50 grids.

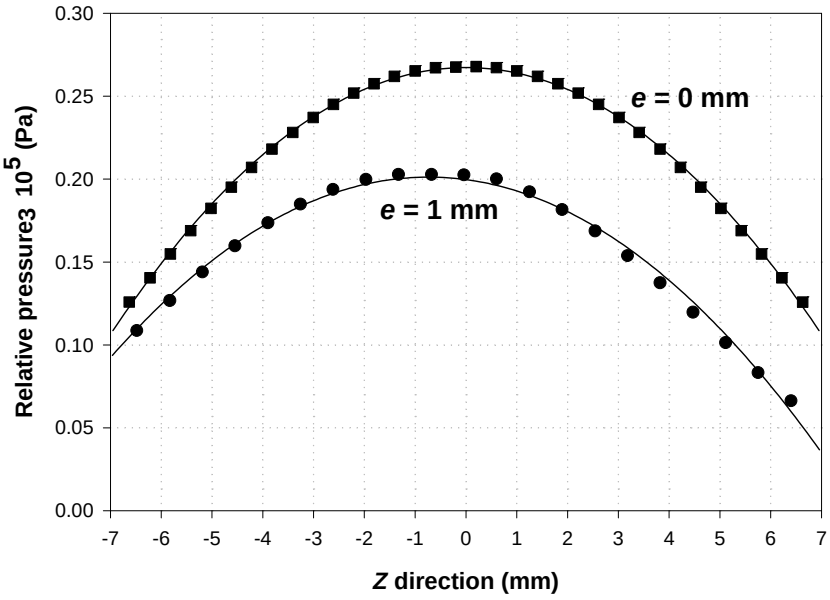

Figure 10: Profiles of the relative pressure, along z direction at mid-plane between the upper and lower jet exit for V_0 = 0.45 m/s, H = 13 mm, d = 14 mm, e = 1 mm with 80 × 80 × 50 grids.

CONCLUSIONS

A mathematical model describing the 3D counterflow diffusion flames has been solved by combining the CHEMKIN thermodynamical and transport data bases with the commercial CFX software. Eccentricity along z-axis direction between the upper oxidiser nozzle and lower fuel nozzle was used to reflect the misalignment of the counterflow burner. The assumption of constant $1/r(\partial p/\partial r)$ proposed by Kee et al.[7] is not valid for flames produced in a misalignment burner.

The flame becomes narrower along the eccentricity direction (or z-axis direction) but remains unaffected along y direction at the mid-plane between the upper and lower duct exits. The difference between the axial velocity profiles for e = 0 and e = 1 is negligible, with the maximum heat release moving closer toward the mid-plane as the eccentricity increases. The maximum variation in the axial temperature profile due to misalignment is less than 100 K for cases considered in this study, suggesting that those profiles are weakly sensitive to the alignment. However, the radial profiles of temperature, velocity components and species concentrations are very sensitive to torch alignment.

NOMENCLATURE

A	pre-exponential factor; [m^6/mol^2] for the one global reaction
a	radius of the jet; [m]

C_1, C_2, C_3, C_μ	k-ε equation constants
d	burner duct diameter; [m]
E_a	activation energy; [J/(mol K)]
e	eccentricity; [m]
G	G denotes production of the turbulent kinetic energy (k) and turbulent dissipation rate (ε) due to body force; [kg/(m s^3)]
H	separation gap between the upper and lower duct exits; [m]
h	enthalpy; [J/kg]
k	turbulent kinetic energy; [J/kg]
P	P is the shear production in k-ε equations; [kg/(m s^3)]
p	pressure; [Pa]
R	reaction rate; [mol/(m^3 s)]
r	radial coordinate; [m]
r_∞	radius of the computational domain; [m]
S_ϕ	source term in the conservation equations
T	temperature; [K]
t	time; [s]
V_0	jet velocity; [m/s]
V_x, V_r and V_θ	velocity components in the axial, radial and azimuthal directions; [m/s]
V_y and V_z	velocity component in the y and z directions; [m/s]
W_i	molecular weight for species i; [kg/mol]
x	axial coordinate; [m]
ε	turbulent energy dissipation; [m^2/s^3] or [J/(kg s)]
ϕ	conserved variable
Γ_i	species diffusivity; [Pa s]
Γ_ϕ	arbitrary variable diffusion coefficient; [Pa s]
μ	effective viscosity; [Pa s]

μ_m	dynamic viscosity; [Pa s]
μ_T	turbulent viscosity; [Pa s]
κ	von Kármán constant
θ	azimuthal coordinate; [rad]
ρ	density; [kg/m^3]
σ_i	species turbulent Prandtl number
ψ	stream function; [m^2/s]

REFERENCES

1. AEA Technology (1995) *CFX-4.2: Solver Manual*.

2. Bedat B., Egolfopoulos F. N. and Poinsot T. (1999) "Direct Numerical Simulation of Heat Realease and NO_x Formation in Turbulent Nonpremixed Flames", *Combustion and Flame* **119**, 69-83.

3. Chung S. L. and Katz J. L. (1985) "The Counterflow Diffusion Flame Burner: A New Tool for the Study of the Nucleation of Refractory Compounds", *Combustion and Flame* **61**, 271-284.

4. Dixon-Lewis G. (1990), 23rd *Symposium (International) on Combustion* 305-324.

5. Fristrom R. M. (1995) *Flame Structure and Processes*, Oxford University Press.

6. Frouzakis C. E., Lee J., Tomboulides A. G. and Boulouchos A. (1998) "Two-Dimensional Direct Numerical Simulation of Opposed-Jet Hydrogen-Air Diffusion Flame", *27th Symposium (International) on Combustion* 571-577.

7. Kee R. J., Miller J. A., Evans G. H. and Dixon-Lewis G. (1988) "A Computational Model of the Structure and Extinction of Strained, Opposed Flow, Premixed Methane-Air Flames", *22nd Symposium (International) on Combustion* 1479-494.

8. Kitajima A., Ueda T., Matsuo T., and Mizomoto M. (2000) "A Comprehensive Examination of the Structure and Extinction of Turbulent Nonpremixed Flames Formed in a Counterflow", *Combustion and Flame* **121**, 301-311.

9. Kostiuk L. W., Bray K. N. C., and Cheng R. K. (1993) "Experimental Study of Premixed Turbulent Combustion in Opposed Streams. Part II - Reacting Flow Field", *Combustion and Flame* **92**, 396-409.

10. Lindstedt R. P. and Vaos E. M. (1999) "Modelling of Premixed Turbulent Flames with Second Moment Methods", *Combustion and Flame* **116**, 461-485.

11. Lutz A., Kee R. J., Grcar J. F. and Rupley F. M. (1997) *OPPDIF User Manual*, SAND96-8243.

12. Potter A., and Butler J. (1963) "Apparent Flame Strengths*", 8th Symposium (International) on Combustion* 1027-1034.

13. Rogg B. (1988) "Response and Flamelet Structure of Stretched Premixed Methane-Air Flames", *Combustion and Flame* **73**, 45-65.

14. Sung C. J., Liu J. B., and Law C. K. (1995) "Structural Response of Counterflow Diffusion Flames to Strain Rate Variations", *Combustion and Flame* **102**, 481-492.

15. Takagi T., Yoshikawa Y., Yoshida K., Komiyama M. and Kinoshita S. (1996) "Studies on Strained non-Premixed Flames Affected by Flame Curvature and Preferential Diffusion", *26th Symposium (International) on Combustion* 1103 -1110.

16. Versteeg H. K. and Malalasekera W. (1995) *An Introduction to Computational Fluid Dynamics: The Finite Volume Method*, Longman Group Ltd.

17. Yan Z. and Holmstedt G. (1999) "Three-Dimensional Computation of Heat Transfer from Flames Between Vertical Parallel Walls", *Combustion and Flame* **117**, 574-588.